Journal of Sol-Gel Science and Technology (2021) 100:55–67
https://doi.org/10.1007/s10971-021-05635-6

ORIGINAL PAPER: FUNCTIONAL COATINGS, THIN FILMS AND MEMBRANES (INCLUDING DEPOSITION TECHNIQUES)

Modification of surface morphology and lattice order in nanocrystalline ZnO thin films prepared by spin-coating sol–gel method

R. Gegova-Dzhurkova[1] · D. Nesheva[1] · V. Dzhurkov[1] · M. Šćepanović[2] · M. Grujić-Brojčin[2] · I. Bineva[1] · V. Mihailov[1] · Z. Levi[1] · E. Manolov[1] · Z. V. Popović[2]

Received: 28 May 2021 / Accepted: 25 August 2021 / Published online: 16 September 2021

Abstract

The surface morphology and structure of zinc oxide thin films play a key role in many applications such as chemical sensors and photocatalysts. In this study, ZnO thin films are prepared on Si/SiO_2 substrates by spin-coating sol–gel technique. New element in the films preparation is the application of drying with hot air flow (T_h= 90–95 °C), as first step of the drying procedure, followed by furnace drying as second step. It is shown that hot air drying has significant influence on the films properties. It reduces the internal stress, strongly affects the films surface morphology, gives assistance to the effusion of organic remains and results in a better crystallinity and lower defect density in the as-prepared films when compared with the films prepared by furnace drying only. Besides, first data on the modification of sol–gel ZnO films by post-deposition irradiation with a nanosecond infrared laser are obtained, giving an alternative to the standard furnace annealing. They indicate that laser irradiation of as-prepared ZnO films gives rise to certain improvement in crystal structure and slight increase in crystallite size, followed by the increase of micro-strain. It also reduces the number of defects playing role of non-radiative recombination centers, as well as the size and density of small cracks and pores on the surface of as-prepared films.

Graphical Abstract

Left: X-ray diffraction patterns of as-prepared and annealed at 400 °C ZnO films prepared by furnace drying only, the patterns are taken on non-irradiated and laser-irradiated films. Middle: Experimental and fitted E_2^{high} Raman mode in the spectra of non-irradiated and laser-irradiated samples prepared by two-step drying, *as* - the asymmetry fitting parameter.

Supplementary information The online version contains supplementary material available at https://doi.org/10.1007/s10971-021-05635-6.

✉ D. Nesheva
nesheva@issp.bas.bg

[1] G. Nadjakov Institute of Solid State Physics, Bulgarian Academy of Sciences, 72, Tzarigradsko Chaussee Blvd, 1784 Sofia, Bulgaria

[2] Center for Solid State Physics and New Materials, Institute of Physics, University of Belgrade, Pregrevica 118, Belgrade 11080, Serbia

Right: Optical and AFM surface images of annealed ZnO films prepared by one-step drying; the AFM images were obtained at two different scales.

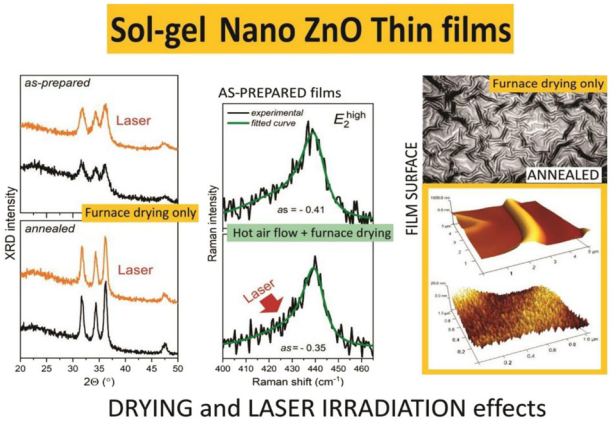

Keywords Sol–gel · Drying · ZnO nanostructured layers · Laser irradiation · Surface morphology · Lattice strain

Highlights

- Zinc oxide thin films of densely packed nanograins are prepared by sol–gel method.
- Hot air drying during films preparation and post-deposition infrared laser irradiation are applied.
- The hot air drying has strong influence on the internal strain and surface morphology.
- The laser irradiation reduces the size and density of pores and cracks on the surface.
- Defect density decreases but internal strain increases upon the laser annealing.

1 Introduction

Zinc oxide (ZnO) is a semiconductor, which has been widely studied in physics, chemistry, material science, biochemistry, etc. and has already found a number of applications. It is used in the ceramic, rubber and concrete industry, sunblock creams, food, etc [1]. In thin film form ZnO has attracted significant interest due to its potential applications in optoelectronics, transparent electronics, as surface acoustic wave devices, resistive gas sensors and photocatalists, transparent conductive electrodes and solar cell windows, etc [2–6]. Various methods are applied for thin film preparation as the method of deposition is usually chosen taking into account the requested films properties and the cost of the method. When intended applications require precise control of the growth process and production of high purity materials molecular beam epitaxy, metalorganic chemical vapor deposition, magnetron sputtering [7], or atomic layer deposition [8] are used. However, these techniques are based on usage of dedicated and usually costly and complicated equipment. Various chemical techniques are also used for growing ZnO thin films, such as spray pyrolysis, sol–gel, hydrothermal process, electrodeposition, inkjet printing [9–13]. These techniques are easier and cost-effective than vapor deposition methods, since they do not require vacuum equipment and ultrapure chemical elements or gases. When using some of them (hydrothermal method [10, 11], sol–gel method [12, 13]) the synthesis of zinc oxide films takes place at low temperatures. The sol–gel method is one of the most straightforward chemical techniques for ZnO thin film preparation which has the advantage of coating on large areas with easy control of the doping level without using expensive and complicated equipments [12]. The sol composition and other preparation conditions may be varied to prepare films with different properties. In particular, the morphology of the films after the drying process is strongly influenced by the drying parameters [13] and it is essential to find proper drying conditions for each application.

Postdeposition treatments of chemically deposited films, such as conventional furnace annealing and rapid thermal annealing, are normally applied, as they play significant role in improving the crystalline quality and modifying film properties. Recently, laser irradiation has emerged as an effective method for modification of surfaces and structure of metal oxides [14]. It possesses some advantages in comparison with the thermal annealing methods - fast crystallization at room temperature, rapid local heating and possibility of local crystallization and low influence on the substrate. A comparison of the effect of postdeposition irradiation for 5 min of ZnO films by cw Ar^{+} laser (wavelength $\lambda = 514$ nm) with the result of thermal annealing at

500 °C for 60 min, has shown [15] that the laser irradiation was more effective in both modifying the surface morphology and relaxing the residual compressive stress in the as-grown films. The influence of the laser treatment of as-prepared sol–gel ZnO thin films by KrF excimer laser [16] on the film crystallinity, microstructure, surface morphology and optical transmittance was compared to the results of thermal annealing of the films. It has been obtained that the level of crystallinity of the laser annealed films is higher and the average crystallite size was greater than those of the thermally annealed ones. The crystallinity improvement and the average crystallite size of the laser-irradiated ZnO films increased with the fluence increase. The effect of laser irradiation on the electrical properties of pure and Al-doped ZnO films was also explored by several research groups [17–19]. It has been shown [18] that the irradiation of ZnO films by pulse infrared laser ($\lambda = 1064$ nm, pulse width 5 ns and pulse energy of 0.8 J) resulted in improvement of the electrical properties of the films and reduction of the grain size.

In this study ZnO thin films were prepared on Si/SiO_2 substrates by spin-coating sol–gel technique and a part of them were post-deposition furnace annealed at 400 °C. A way for modification of nanocrystalline zinc oxide thin films is proposed in which the important new element is application of drying with hot air flow ($T_h = 90$–95 °C), as first step of the drying procedure. Post-deposition irradiation with a nanosecond infrared laser is also used for films modification, as an alternative of the standard furnace annealing. X-ray diffraction, optical microscopy, atomic force microscopy, scanning electron microscopy and Raman scattering technique were used to study the effect of each kind of treatment on the morphological and structural modification of the films.

2 Experimental procedures

2.1 Sample preparation

Zinc oxide thin films were prepared by sol–gel method using the spin-coating technique. The films were deposited in a single step by rotating the substrates for 30 s at a rate of 2800 rpm. Zinc acetate heptahydrate ($Zn(CH_3COO)_2{\cdot}7H_2O$, ≥99.5%) dissolved in 99.97% ethanol (C_2H_5OH, 99.97%) was used for the preparation of 0.5 M solution. During the homogenization, monoethanolamine (MEA)(C_2H_7NO) was added to the solution as stabilizing agent [20]. For complete homogenization, the solution was heated up to 45 °C and stirred on a magnetic stirrer for 45 min and then it was aged for 24 h before the film preparation. The films were deposited on crystalline c-Si substrates covered with 300 nm thick SiO_2 film grown by thermal wet oxidation. Before the film deposition the substrates were cleaned with a $H_2O_2 + NH_4OH$ solution, washed in C_2H_5OH (99.97%) and finally ultrasonically treated for 20 min in ethanol (99.97%).

Two groups of as-prepared samples were produced by using either the standard one-step drying procedure [21, 22] i.e., furnace heating in static air at 140 °C (413 K) for 10 min immediately after layer deposition (group I, samples I-1) or a two-step drying procedure (group II, samples II-1); the II-1 samples were first dried for 5 min with a hot air flow (temperature $T_h = 90$–95 °C (363–368 K)) with volume flow rate of 7.5 l/s and then furnace dried at 140 °C for 10 min. The air flow was perpendicular to the sample surface. Two other groups of samples (I-2 and II-2) were prepared by postdeposition annealing of some as-prepared samples from groups I-1 and II-1 at 400 °C (673 K) for 60 min in static air (below called annealed films). Spectroscopic ellipsometry measurements have shown [23] that the film thickness is in the range 250–450 nm as the thickness of the annealed films is considerably smaller (of 30–40%) than that of the corresponding as-deposited films. This observation has been related to decrease of film porosity and effusion of the organic residues. The sample preparation conditions are described in Table 1.

Samples from each group were laser beam irradiated at room temperature in air on a circle spot with an area of ≈0.25 cm^2. Q-switched Nd:YAG laser (Quanta Ray GCR3, $\lambda = 1064$ nm) was used operated at 10 or 20 Hz and the total number of laser pulses was varied in the range $N = 100$–4000. For all samples the laser fluence was $f \approx 100$ mJ/cm^2.

Table 1 Description of the film preparation steps and laser irradiation conditions

Sample group	Preparation steps	Number of applied laser pulses, N
I-1	One-step furnace drying, 140 °C, 10 min	4000
I-2	One-step furnace drying, 140 °C, 10 min Furnace annealing, 400 °C, 60 min	100 or 4000
II-1	Two-step drying comprising: • hot air drying, 5 min • furnace drying, 140 °C, 10 min	100, 300 or 4000
II-2	Two-step drying (see above) Furnace annealing, 400 °C, 60 min	600 or 4000

2.2 Sample characterization

The crystal structure of ZnO films was investigated by X-ray diffraction (XRD) measurements performed by a PANalytical Empyrean diffractometer using the Cu Kα line ($\lambda_{K\alpha} = 1.5406$ Å (0.15406 nm)).

The surface morphology and crystallite grain size and shape were investigated by atomic force microscopy (AFM) using a Multi Mode V microscope (Bruker, ex. Veeco, Santa Barbara, CA), as well as by scanning electron microscopy (SEM) using a JEOL JSM 6390 microscope (operated at 20 kV, magnification ×10,000, ×20,000, and ×30,000). The AFM images were taken in tapping mode on scales of 1 µm and 5 µm. Aluminum coated silicon cantilevers TAP150-Al-G (Budget Sensors Innovative Solutions Bulgaria Ltd.) with resonant frequency of 150 kHz and spring constant of 5 N/m were used. The radius of the cantilever's tip is smaller than 10 nm. The images were just flattened and no further processing was performed. The image analysis was done by means of Nanoscope 7.30 program.

Raman spectroscopy was applied in order to obtain information on the crystallinity of ZnO films as well as the organic remains. The Raman scattering measurements have been performed by using TriVista TR557 triple spectrometer system equipped with a liquid nitrogen-cooled CCD detector. All samples were measured in backscattering micro-Raman configuration using 514.5 nm line of a mixed Ar^+/Kr^+ ion laser with the output laser power in the range of 20–100 mW. To record the spectra of relatively high resolution in the wavenumber range (70–660 cm^{-1}) where characteristic ZnO Raman modes could appear, 900/900/1800 groves/mm diffraction grating combination was used in the TriVista system. These spectra were obtained using objective lens with ×100 magnification which focuses the laser beam to a spot size of about 2 µm. The application of this objective gives a laser power on the sample surface of about 4 mW at a laser output power of 100 mW. To suppress very intense Raman mode of silicon substrate at 520.6 cm^{-1} parallel polarization of incident and scattered light has been chosen and the samples were oriented to provide minimum intensity of that mode in the spectra of ZnO films. The as-measured Raman spectra were corrected by subtracting the spectra originating from Raman scattering on N_2 in the air, in order to better distinguish the Raman modes associated with crystalline ZnO in the range below 120 cm^{-1}. Thus, corrected spectra were shifted to center the most intensive mode of crystalline silicon from the substrate at exactly 520.6 cm^{-1}. In this way the error in determining the mode shift attributed to ZnO has been set to less than ±0.3 cm^{-1}. On the other side, the spectra that should provide the information on the properties of organic remains were measured in a wide wavenumber range (600–4100 cm^{-1}) using 300/300/500 grooves/mm grating combination, objective with ×50 magnification giving a laser spot size of around 4 µm, and power less than 2 mW at the sample surface (at output laser power of 50 mW). All spectra were recorded in the air, at room temperature, with the accumulation time of 600 s. The representative spectra were obtained by averaging several (up to 4) individual spectra collected at the same measuring point of each sample. Optical images of the film's surface were also obtained with the confocal microscope of the micro-Raman system using objective lens with the ×100 magnification.

3 Results and discussion

XRD patterns of as-prepared and annealed ZnO produced by applying one-step or two-step drying are shown in Fig. 1. X-ray diffraction patterns of laser irradiated samples are also shown in Fig. 1. The broad band with maximum at $2\Theta \sim 23^{o}$ is due to diffraction from the 300 nm thick amorphous SiO_2 film situated between the crystalline silicon substrate and ZnO layer [24]. Four characteristic peaks of crystalline ZnO with wurtzite structure (JCPDS No.36-1451) are also observed in the spectra of all samples.

It is known [20] that MEA controls the rate of condensation reactions in the sol by competing with negatively charged hydroxyl- or alkoxy- groups (OH-, Ak-), and this leads to uniform gelling of the layer. It absorbs to positively charged facets of Zn-complexes thus facilitating their coordination and condensation. Therefore, the observed good crystallinity of the as-prepared ZnO samples (I-1 and II-1) is most likely due to the presence in the solution of Monoethanolamine as stabilizing agent.

A comparison of the XRD patterns of as-prepared and annealed films in each group shows that the XRD peaks in the spectra of annealed films are stronger and slightly narrower than the bands in the XRD spectra of the corresponding as-prepared films. These results show that, as expected [25], furnace annealing of the films at 400 °C causes an improvement of the crystallinity of as-prepared films. Comparing the XRD patterns of the as-prepared films made by using one-step and two-step drying (I-1 and II-1, respectively) one can notice that the XRD peaks in the spectrum of the II-1 sample related to ZnO are stronger than those in the spectrum of the sample I-1; the patterns of the annealed films (I-2 and II-2) are very similar. This means that the usage of hot air treatment resulted in a better crystallinity of the as-prepared films, but it has not appreciable effect on the crystallinity of films annealed at 400 °C. The XRD patterns in Fig. 1 indicate that the laser irradiation of films prepared by the conventional furnace drying improves the crystallinity of

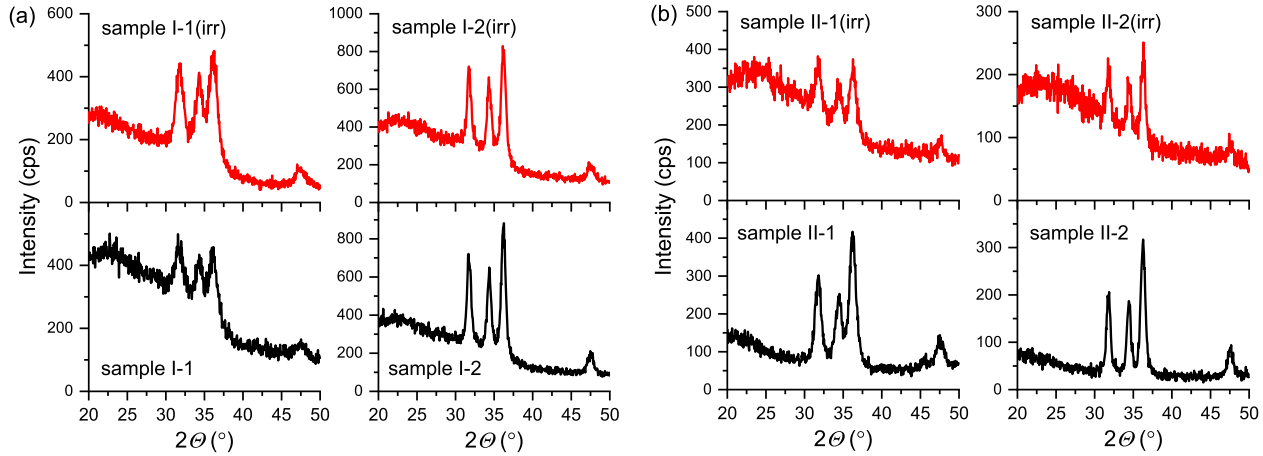

Fig. 1 XRD patterns of non-irradiated (bottom curves) and laser-irradiated (top curves) ZnO films. The films **a** furnace dried at 140 °C and **b** prepared by using hot air drying as first step and furnace drying at 140 °C as second step. The samples I-1 and II-1 are as-prepared, I-2 and II-2 are further annealed at 400 °C

as-prepared films, but no significant laser-induced structural change is observed in the annealed film. The effect of laser irradiation on the films crystallinity is weaker than that of the furnace annealing at 400 °C for 60 min. A comparison with the data reported in the literature shows that the energy transferred to the ZnO films by the infrared laser irradiation applied in this study is relatively low, which could explain the relative weak laser irradiation effect.

In order to estimate the lattice parameters, crystallite size, and strain, the segment of the XRD patterns in the $2\Theta = 29°–39°$ range was decomposed into three Lorentzians (Supplementary material 1). The results of performed analysis of XRD measurements data of I and II sample groups, both non-irradiated and laser-irradiated, is given in Table 2. Presented results include lattice parameters (a, c), crystallite size D and the strain ε_{cc} and ε_{aa} along c-axis and a-axis, respectively, *for* all analyzed samples. The lattice parameter a for $\langle 100 \rangle$ plane is calculated by $a = \lambda/\sqrt{3}\sin\Theta$, while the lattice constant c for $\langle 002 \rangle$ plane is calculated by $c = \lambda/\sin\Theta$, where Θ represents the position of the diffraction peaks corresponding to a given crystalline plane [26]. The crystallite size D, given in the Table 2, is calculated by averaging the values obtained for three of the most intensive diffraction peaks according to Sherrer's equation $D = K\lambda_{K\alpha}/\beta\cos\Theta$, where the value 0.94 is used for the shape factor K and β is full width at half maximum of the diffraction peaks. The values of homogeneous strain along a- and c-axis for each sample are calculated by the strain equations $\varepsilon_{aa} = \frac{a-a_0}{a} \times 100\%$ and $\varepsilon_{cc} = \frac{c-c_0}{c_0} \times 100\%$, respectively [27], where $a_0 = 3.2498$ Å and $c_0 = 5.2066$ Å are relaxed reference parameters for the bulk ZnO (JCPDS No. 36–1451). The detailed analysis is given in Supplementary material 1, together with the results of the Williamson-Hall method applied to the non-irradiated and irradiated samples from group I.

From the results shown in Table 2 it can be seen that the usage of hot air flow leads to slight increase of the crystallite size, from 7.5 nm in I-1 to 9.9 nm in sample II-1. The furnace annealing at 400 °C results in significant increase in the crystallite size, from 7.5 to 14.2 nm in the sample group I, and from 9.9 to 15.7 nm in the sample group II. On the other side, the results presented in Table 2 indicate that laser irradiation has a small effect on the crystallite size of both groups of samples, because the variations of the values shown in Table 2 do not exceed 1 nm. However, it should be noted that the values of crystallite size D from Table 2 are calculated by Sherrer's equation, which does not take into account the influence of microstrain on the broadening of diffraction peaks and this can lead to values of crystallite size D being underestimated.

The results related to lattice parameters a and c, together with corresponding strain values (ε_{aa}, ε_{cc}), show that the samples produced by one-step drying (group I) exhibit the tensile strain along c-axis ($c > c_0$, $\varepsilon_{cc} > 0$). Note that in this group most of the samples also have values of parameter $a > a_0$ ($\varepsilon_{aa} > 0$), with the exception of sample I-1(irr), with a slightly lower than a_0 ($\varepsilon_{aa} = -0.003$) (see Table 2 and Supplementary material 1). Among the samples produced by two-step drying procedure (group II), the strain in sample II-1 is almost relaxed ($c \approx c_0$, $\varepsilon_{cc} \approx 0$), whereas the rest of the samples in this group show compressive strain along c-axis ($c < c_0$, $\varepsilon_{cc} < 0$). The parameter a in the samples of this group is close to reference value. According to this analysis, the process of two-step drying leads to significant relaxation of strain. On the other side, the laser irradiation causes a slight increase of tensile strain along the c-axis in the samples from group I, and more significant increase of compressive strain along the same axis in the samples from group II. Note that a significant increase of strain in the irradiated samples from group II for sure have a role in

Table 2 The lattice parameters (a, c), crystallite size (D) estimated by Sherrer's equation, as well as the strain along a-axis (ε_{aa}) and c-axis (ε_{cc}) of non-irradiated and laser-irradiated ZnO films determined from X-ray diffraction data

Sample group	Non-irradiated samples					Laser irradiated samples				
	Lattice parameters (Å)		D (nm)	Strain		Lattice parameters (Å)		D (nm)	Strain	
	a	c		ε_{aa} (%)	ε_{cc} (%)	a	c		ε_{aa} (%)	ε_{cc} (%)
I-1	3.2523(7)	5.219(1)	7.50 ± 0.08	0.08 ± 0.02	0.24 ± 0.02	3.2488(4)	5.2213(8)	7.65 ± 0.08	−0.03 ± 0.01	0.28 ± 0.02
I-2	3.2514(3)	5.2149(5)	14.2 ± 0.1	0.049 ± 0.009	0.16 ± 0.01	3.2512(3)	5.2158(5)	13.6 ± 0.1	0.043 ± 0.009	0.18 ± 0.01
II-1	3.2499(5)	5.2066(10)	9.9 ± 0.1	0.00 ± 0.02	0.00 ± 0.02	3.2499(9)	5.201(2)	10.3 ± 0.2	0.00 ± 0.03	−0.11 ± 0.04
II-2	3.2475(4)	5.2052(7)	15.7 ± 0.2	−0.07 ± 0.01	−0.03 ± 0.01	3.2484(8)	5.199(1)	14.9 ± 0.3	−0.04 ± 0.02	−0.15 ± 0.02

XRD peak broadening, but this is not taken into account in the estimation of crystallite size D (Table 2), because it has been calculated by Sherrer's equation. In this way, certain increase in crystallite size D due to laser irradiation may not be fully detected from the results shown in Table 2.

Optical surface images of three samples (I-2, II-1, and II-2) subjected to different drying and annealing procedures are displayed in Fig. 2; the image of sample I-1 (not shown) is similar to the image of sample I-2. The images show that the surface morphology of the films from group I (I-1 and I-2) prepared by using one-step drying (Fig. 2a) is very different from that of the group II films (II-1 and II-2) prepared by applying two-step drying procedure (Figs. 2b and c). Fiber-like features (stripes, wrinkles) are seen on the surface of the films from group I and the image in Fig. 2a shows that the film annealing does not remove wrinkles formed during the drying process. The surface of the two samples prepared by using two-step drying is uniform. Wrinkling has been observed by other authors on the surface of undoped [13, 28] and doped [29, 30] ZnO thin films.

Stripes can appear during the spin-coating or drying process. Throughout the entire spin-coating process evaporation of sol solvents occurs and a concentration profile is developed within the thinning fluid to feed the evaporation at the top surface [31]. Since the nonvolatile components are not removed, there should be a build-up of these solutes near the fluid/vapor interface. This could increase solute concentration at the fluid surface and lead to a local increase in the fluid viscosity and formation of a "skin" layer, which may restrict the subsequent solvent evaporation. In our case, all liquid films were prepared on the substrates at same deposition conditions. Hence, their surface morphology is determined by the drying process applied rather than by the formation of a surface "skin" during the spin-coating process.

The shrinkage of the films due to residues evaporation causes various levels of internal stress inside the films. Depending on the evaporation rate and the stress-specific patterns can appear on the film surface. Thus, the morphology of the films after the drying process is strongly influenced by the drying procedure [13]. Thermogravimetric-differential thermal analysis of Zn-sol with 2-methoxyethanol as solvent (boiling temperature 124 °C) has shown [13] that when heating at a rate of 10 K/min the weight loss till ~80 °C was ~55% and the loss in 80–220 °C region was ~15%. The boiling temperature of ethanol at atmospheric pressure is ~78 °C while MEA evaporation takes place at ~120 °C. One can assume that during the one-step isothermal furnace drying at 140 °C in static air the weight loss and physical shrinkage is fast and this could result in high lattice disorder in the as-prepared films. When applying the two-step drying procedure during the first step (treatment with hot air (90–95 °C)) the solvent evaporation may be retarded by the air flow directed to the film surface

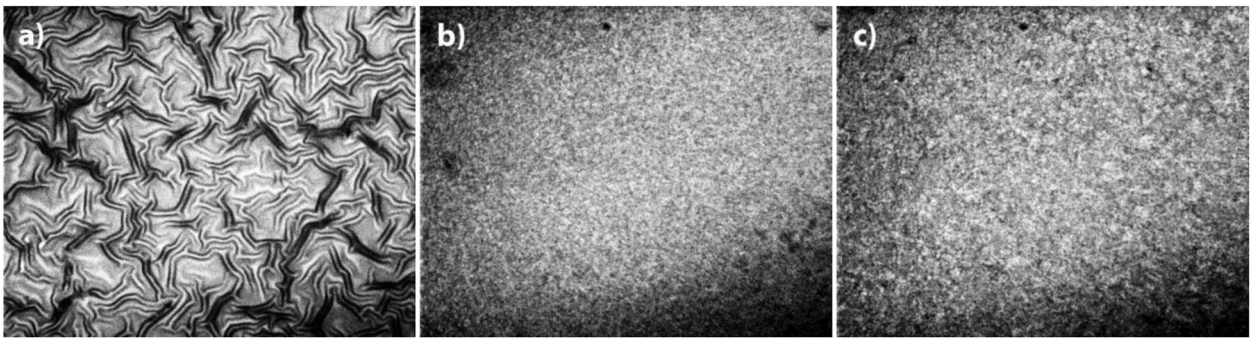

Fig. 2 Optical images of the surface of two samples annealed at 400 °C: **a** sample I-2 and **b** sample II-2; **c** optical image of as-deposited sample II-1, prepared by applying the two-step drying procedure. The micrographs were recorded under the ×100 magnification objective of optical microscope coupled to the Raman spectrometer and presented the sample area of about 50 µm wide

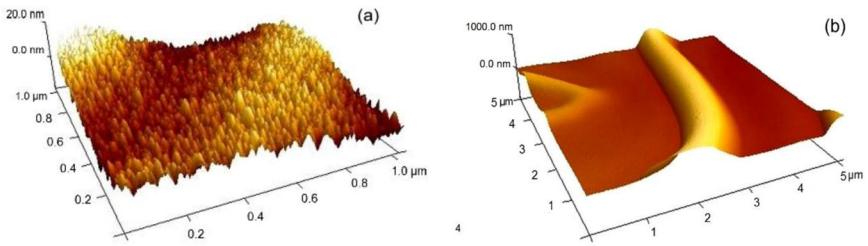

Fig. 3 Three-dimensional surface images of sample I-2 obtained at 1 µm (**a**) and 5 µm (**b**) scale. Please pay attention that z-scales in figures **a** and **b** are very different

which would result in slower shrinkage and better lattice ordering (shown by the XRD results in Fig. 1). In addition, the hot air treatment may facilitate oxygen absorption in the layer thus reducing density of oxygen vacancies and having contribution to lattice ordering. The annealing at high temperature (400 °C) effectively increases lattice order and therefore both types of annealed films display similar XRD patterns.

The mechanisms proposed for explanation of surface wrinkling are based on assumption for creation of internal stress in the sol during drying. According to the mechanism suggested in ref. [20]. when the stabilizer is of high volatility, instability and vapor pressure, a dried layer is initially formed at the film/air interface and extends to the lower part of the film with drying time. Meanwhile, the expansion coefficient of the bottom (wet) layer increases, the capillary force of liquid phase decreases and an upward force is generated at the bottom layer that transfers through the dried layer and causes surface wrinkling. For sols with Monoetholamine (having high evaporation rate) this type of morphological features have been related [28, 32] to rapid MEA evaporation which stimulates a fast course of hydrolysis-condensation reactions and release of hydroxyl- or alkoxy-groups from the volume of the film that leads to appearance of internal stress between the substrate and the ZnO-sol.

To get more information about the size and microstructure of the stripes seen in Fig. 2a. AFM measurements were carried out. Two three-dimensional (3D) AFM surface images of sample I-2 obtained at 1 µm (a) and 5 µm (b) scale are shown in Fig. 3. It is seen from Fig. 3a that the film consists of densely packed grains, and no clustering is observed. The image analysis has shown that the grain size is in the range 15–30 nm. It is larger than the size of ~15 nm determined from the XRD results. This difference can be due to the above-discussed underestimation of the grain size, as well as to the convolution of the tip of the probe with the grain resulting in size overestimation. Stripes of very different height (from a few tens nanometers to several hundred nanometers) are observed in Fig. 3. A stripe of a small height is seen from Fig. 3a which has identical microstructure with the microstructure in the valleys. This supports the above suggestion that the appearance of surface stripes is due to relaxation of the internal stress in the layer rather than to growth of features with different microstructure and composition. Based on this assumption the uniform surface of the films prepared by two-step drying (Fig. 2b, c) can be related to lower level of internal stress in these films. Hence, the application of hot air drying reduces the internal stress in the ZnO films thus having strong effect on the surface morphology.

Comparing the optical images of the surface of non-irradiated and laser-irradiated samples prepared by conventional furnace drying at 140 °C and annealed at 400 °C we have found some indication that, although laser irradiation does not change significantly crystallinity and crystallite size of the films (see Fig. 1, sample I-2), it causes

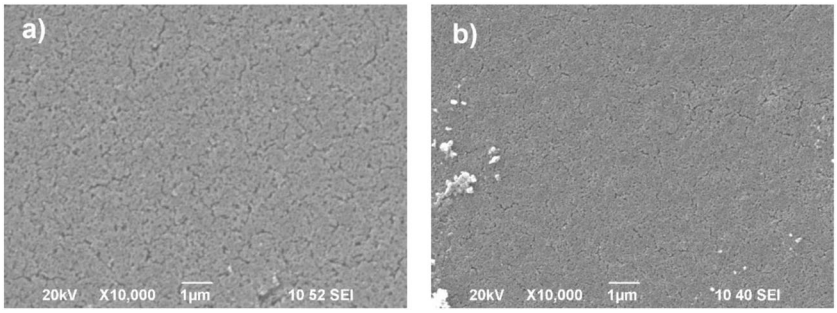

Fig. 4 SEM images of two II-1samples prepared by applying the two-step drying procedure: **a** non-irradiated ZnO film, **b** laser irradiated ZnO film, $N = 100$

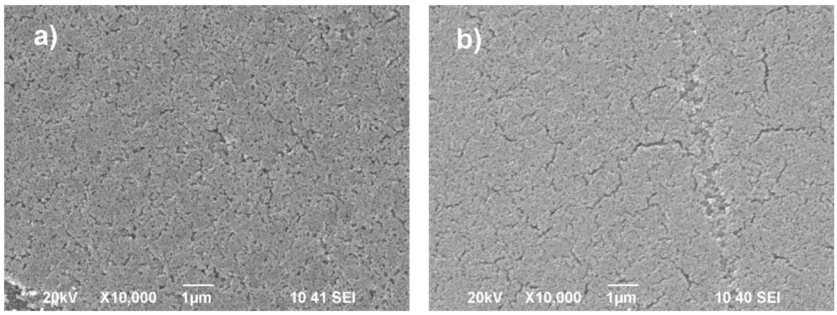

Fig. 5 SEM images of two II-2 samples post deposition annealed at 400 °C: **a** non-irradiated ZnO film, **b** laser irradiated ZnO film, $N = 600$

some additional wrinkling of the surface. This observation requires further investigations and could be interesting from chemical sensing and photocatalytic points of view.

Additional information about the effect of laser irradiation and hot air flow on the film properties was obtained by SEM and Raman scattering techniques. SEM images of non-irradiated and laser-irradiated as-prepared (II-1) and annealed (II-2) ZnO thin films prepared by using two-step drying are displayed in Figs. 4 and 5, respectively; no results for the films from group I are shown because they are influenced by the wrinkles on the film surface. It is seen that the surface of non-irradiated as-prepared (Fig. 4a) and annealed (Fig. 5a) type II layers has a considerable porosity, short narrow cracks are also visible. The density of cracks on the surface of the annealed film is a little higher than that on the surface of the as-prepared one. After laser irradiation ($N = 100$) the surface of film II-1 looks more compact and the density of pores and cracks is significantly reduced (Fig. 4b). The irradiation of the annealed film II-2 ($N = 600$) makes the cracks longer and wider (Fig. 5b).

During the laser irradiation ($\lambda = 1064$ nm, quantum energy 1.16 eV) the beam penetrates to the substrate since the optical band gap of ZnO is 3.3 eV [33]. A part of the energy of the laser beam is transferred to the film, as well as to the Si substrate. It may be converted into heat and thus the laser irradiation may cause film annealing. The irradiation with 100 pulses probably causes a mild annealing that reduces the existing internal stress and makes the film surface more relaxed and smooth. The higher crack density on the surface of non-irradiated and irradiated ($N = 600$) annealed films II-2 is probably due to the big difference in the volume thermal expansion coefficients of nano-ZnO ($1.57 \times 10^{-5}\,K^{-1}$ [34]) and the SiO_2 layer (300 nm thick) underneath ($5.6 \times 10^{-7}\,K^{-1}$ [35]).

Raman scattering spectra of non-irradiated and laser beam irradiated samples selected from groups I and II, together with the spectrum of Si-substrate, in the 70–600 cm^{-1} wavelength range, are shown in Fig. 6. In addition to the Raman modes associated with crystalline silicon from substrate, which include the most intense mode at 520.6 cm^{-1} and second-order 2TA mode of less intensity at about 302 cm^{-1}, the spectra of ZnO films are dominated by two Raman features which can be associated to crystalline ZnO. These features at ~100 cm^{-1} and ~439 cm^{-1} can be assigned to nonpolar phonon modes E_2^{low} and E_2^{high}, mainly associated with the vibrations of the Zn and O atoms in wurtzite ZnO crystal lattice, respectively [36–38]. The position, linewidth and shape of these modes depend on nanocrystallites size, strain, disorder and defects in ZnO nanostructures [36]. The decrease of nanocrystallite size and increase of disorder lead together to the broadening of Raman modes. Although E_2^{high} mode in crystalline ZnO is asymmetric due to anharmonicity, recent studies have shown that phonon confinement effect due to nanocrystallite size [36] could cause additional asymmetrical broadening on the low frequency side of this mode, but without significant impact on its Raman shift, except in the case of nanostructures with dimensions of only a few nanometers [39]. On the other side, the position of the E_2 modes in Raman spectra of ZnO are highly sensitive to microstrain: the tensile strain moves E_2^{high} toward lower frequencies

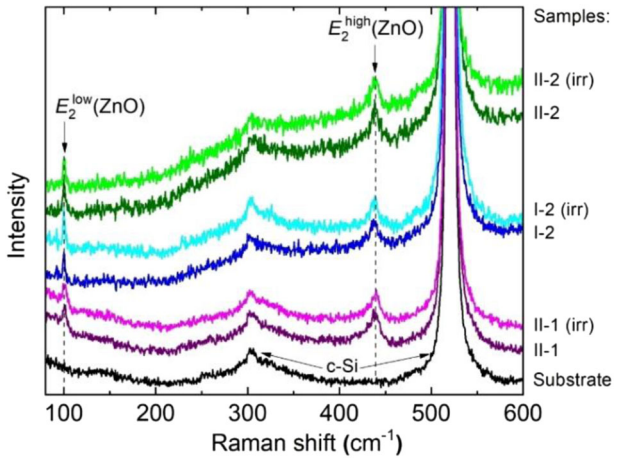

Fig. 6 Raman scattering spectra in the 70–600 cm^{-1} range of non-irradiated and laser-irradiated as-prepared samples from group II-1, and samples from groups I and II annealed at 400 °C. The spectrum of a c-Si/SiO_2 substrate is also shown. All spectra correspond to the same scale, but they are grouped and vertically shifted for clarity

(redshift), whereas the compressive strain has opposite effect (blueshift) [40]. Due to the poor signal-to-noise ratio and very intensive background signal from the substrate in the Raman spectra shown in Fig. 6, it is not possible to conduct a detailed analysis of ZnO modes in a manner similar to that proposed by Šćepanović et al. [36]. Nevertheless, the presented spectra allow several conclusions to be drawn, based on the variation of the position and linewidth of E_2^{low} and E_2^{high} modes in the spectra of samples prepared by different procedures. To estimate these values, E_2^{low} mode has been fitted by the Lorentzian shape, whereas for the fitting of asymmetric E_2^{high} mode, the modified pseudo-Voigt profile has been used, according to the procedure proposed by Korepanov and Sedlovets [41], described in the Supplementary material 2. Obtained results are shown in Table 3.

It can be seen from Table 3 that the E_2^{low} mode has almost the same position (around 100 cm^{-1}) and shape in the spectra of annealed samples (I-2 and II-2). However, this mode is broadened and slightly shifted to higher frequency (~100.5 cm^{-1}) in the spectrum of the as-prepared sample II-1, which, together with somewhat more pronounced E_2^{low} asymmetric tail in this spectrum, indicates the lower crystallinity and higher disorder, due to smaller nanocrystallite size (10 nm) in this film, in comparison with annealed samples (14 and 16 nm). Also, the broadening and increasing of mode asymmetry of the E_2^{high} mode at the lower frequency side in the spectrum of the sample II-1 (which will be explained in details later in the text), could be related to smaller size and lower crystallinity of nanocrystallites. On the other side, significant influence of the microstrain is responsible for different positions (about 438 and 439 cm^{-1}) of the E_2^{high} mode, in two annealed samples (I-2 and II-2, respectively) with the similar nano crystallite size, according to XRD data (see the Table 2). The Raman position of E_2^{high} mode in the spectrum of II-2 is similar to unstrained ZnO crystal, which is in accordance with the low compressive strain registered in this sample. On the contrary, the redshift of this mode in the spectrum of I-2 may be ascribed to significant tensile strain in this film (Table 2). Note that the difference in Raman shifts of ~1 cm^{-1} corresponds quantitatively to different strains registered in these two samples, according to the relation between Raman shift $\Delta\omega$ and strain ε_{cc} along c-axis, $\Delta\omega = m \cdot \varepsilon_{cc}$, where $m = -(527 \pm 28)$ cm^{-1} [42].

The applied fitting procedure enables not only the determination of the position and FWHM of E_2^{high} mode, but also the assessment of the asymmetry which is described by the fitting parameter *as* (see Supplementary material 2 for details). Taking into account the fitting error, the values of parameter *as* obtained for annealed ZnO samples do not deviate much from the literature values for ZnO bulk crystal ($as = -0.22$) [41]. However, the *as* values of −0.41 and −0.36 obtained for the E_2^{high} mode of non-irradiated and laser-irradiated as-prepared samples II-1 and II-1(irr) significantly exceed bulk value (Fig. 7), confirming the additional asymmetrical broadening of this mode due to small nanocrystalite size and/or low crystallinity in these samples. The values of fitting parameters shown in Table 3 have also indicated that E_2^{high} mode in the spectrum of the laser-irradiated as-prepared sample II-1 was slightly blueshifted, narrower and less asymmetric than this mode in the spectrum of nonirradiated sample. The small blueshift of E_2^{high} mode could be related to increased compressive strain due to laser irradiation (registered by XRD data) [41, 42]. On the other side, the narrowing and lower asymmetry of E_2^{high} mode in the sample II-1(irr) imply that laser irradiation has possibly caused a slight increase of nanocrystallites size and crystallinity in as-prepared ZnO two-step dried film, which is not inconsistent with the XRD analysis, having in mind the restrictions of Sherrer's method.

In contrast to the discussed subtle differences in the Raman spectra of as-prepared and annealed samples, as well slight variations of the spectra of as-prepared sample due to laser irradiation, indicating differences in their nanostructures, the spectra of non-irradiated and corresponding laser-irradiated samples annealed at 400 °C are very similar (except for insignificant changes in the background signal).

Raman scattering spectra of non-irradiated and laser beam irradiated films, taken in the 2300–4050 cm^{-1} range are shown in Fig. 8. A broad asymmetric band of similar intensity peaked at ~2900 cm^{-1} is seen in the spectra of non-irradiated and laser-irradiated as-prepared films, II-1and II-1(irr). This band is also observed in the spectra of annealed films. It is well resolved in the spectra of non-irradiated and laser-irradiated films prepared by using

Table 3 The frequencies and full widths at half maximum (FWHM) of E_2^{low} and E_2^{high} ZnO Raman modes, together with the fitting asymmetry parameter *as* of the E_2^{high} mode

Samples	E_2^{low}		E_2^{high}		
	Frequency (cm^{-1})	FWHM (cm^{-1})	Frequency (cm^{-1})	FWHM (cm^{-1})	Asymmetry parameter *as*
I-2	100.0 ± 0.1	2.0 ± 0.3	438.0 ± 0.5	10.7 ± 1.6	−0.28 ± 0.08
I-2(irr)	100.0 ± 0.1	2.2 ± 0.4	438.1 ± 0.4	10.2 ± 1.3	−0.25 ± 0.08
II-1	100.5 ± 0.6	4.2 ± 1.2	438.9 ± 0.3	13.7 ± 1.1	−0.41 ± 0.03
II-1(irr)	100.8 ± 0.6	3.9 ± 1.3	439.4 ± 0.3	11.9 ± 0.1	−0.36 ± 0.0
II-2	100.3 ± 0.1	3.1 ± 0.4	439.0 ± 0.5	10.0 ± 1.5	−0.28 ± 0.08
II-2(irr)	100.3 ± 0.1	2.7 ± 0.4	439.1 ± 0.5	10.1 ± 1.2	−0.29 ± 0.08

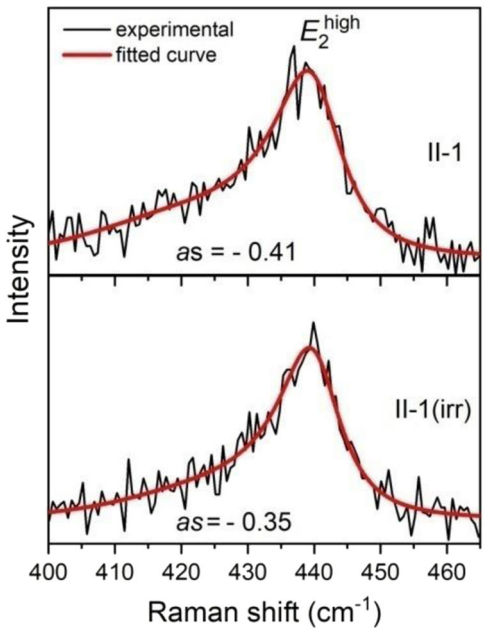

Fig. 7 Experimental and fitted E_2^{high} Raman mode in the spectra of the II-1 and II-1(irr) samples with the asymmetry fitting parameter *as* denoted

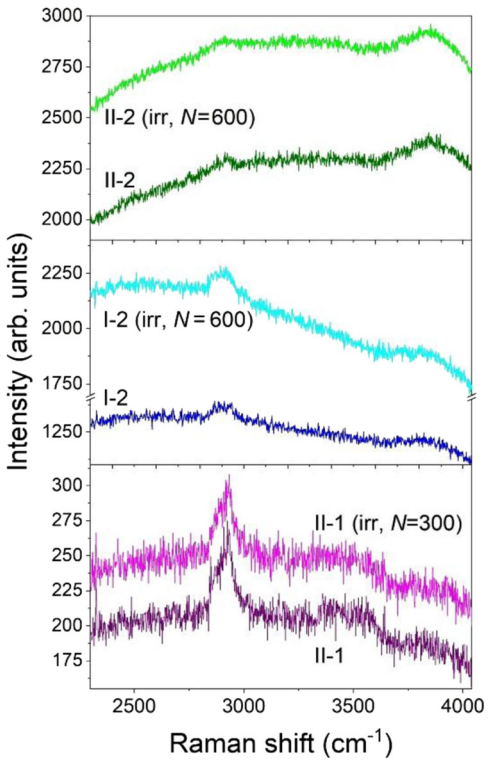

Fig. 8 Raman scattering spectra of non-irradiated and laser beam irradiated samples from group II-1, I-2 and II-2 (*N* – the number of irradiation laser pulses)

one-step drying (I-2 and I-2(irr)), but weak in all spectra of the films from group II, prepared by applying two-step drying procedure. The vibrations in the range 2800–3100 cm^{-1} are assigned to three bands—CH_2 symmetric stretching, CH_3 symmetric stretching, and CH_3 antisymmetric stretching vibration modes [43, 44]. Using the intensity of the band at ~2900 cm^{-1} as a measure for the organic remains in ZnO films one can conclude that: (*i*) the treatment with hot air flow gives some assistance to effusion of organic remains;(*ii*) the laser irradiation did not appreciably affect the process of effusion of organic remains; (*iii*) annealing temperature higher than 400 °C is required for total effusion of remains, which is in agreement with the results of other authors [45, 46].

A second broad band at ~3820 cm^{-1} is observed in the spectra of films annealed at 400 °C but it is more suppressed in the spectra of as-prepared samples. The band is outside of the ranges of the N-H (3300–3500 cm^{-1}) and O-H (3100–3700 cm^{-1}) vibrations [44]. We were unable to identify molecular species responsible for this band. To our opinion, it is not due to Raman vibration modes from organic molecular group. The band is centered at about 1.9 eV and one can assume that it is a photoluminescence (PL) band coming from SiO_2 or ZnO layers. PL band at around 1.9 eV has been observed in the spectra of SiO_2 films and related by many authors to nonbridging oxygen [47–50]. The SiO_2 layer is sandwiched between the c-Si substrate and ZnO layer and the sample annealing was carried out at relative low temperature. Hence, one can expect that SiO_2 layers were not appreciably changed by the sample annealing. However, if the 1.9 eV band is originated only from the SiO_2 layer, this band should be observed in

the same way (similar intensity and shape) in the Raman spectra of all samples, but it is not the case. Therefore, we suppose that the broad band at ~3820 cm^{-1} could rather correspond to red-orange PL from the ZnO layers of the annealed samples. Probably because of the very high defect density in as-prepared ZnO films the non-radiative carrier recombination is dominating and therefore the intensity of ~3820 cm^{-1} band is very low. Observation of red-orange PL band has been reported by a number of authors though it is not very common. Various kinds of lattice defects such as interstitial Zn [51], donor–acceptor defect complexes, including zinc vacancy complexes [52] and oxygen interstitials [53] have been associated with this luminescence. Based on the XRD results we have assumed that the hot air flow treatment facilitates oxygen absorption in the layer thus reducing the density of oxygen vacancies and improving lattice order in the samples from group II. One can assume that a certain amount of interstitial oxygen also exists in these films. It could be responsible for the better expression of the 3820 cm^{-1} band in the spectra of the films prepared by two-step drying. The laser irradiation causes slight increase of this band intensity which could be related to small reduction of the non-radiative recombination centers in the films. Also, the intensity level of all spectra in the range shown in Fig. 8 increases after the laser irradiation, which might be the consequence of the changes in surface morphology induced by laser irradiation and registered by SEM.

In the end, we would like to notice that the treatment with hot air flow caused a strong reduction of the electrical conductivity of the films [23], similarly to the effect of thermal annealing at 400 °C. The laser irradiation also gave rise to irreversible decrease of the electrical conductivity, related to laser-induced reduction of electrically active defects. Non-irradiated and laser-irradiated films prepared by applying two-step drying have shown better sensing response to ethanol vapors at room temperature than the films subjected to one-step drying. These results indicate an enhanced multifunctional performance of ZnO films prepared by treatment with hot air flow or laser irradiated for environmental and other applications.

4 Conclusions

Sol–gel zinc oxide thin films were prepared by spin-coating technique, they consist of densely packed nanosized grains, and no clustering has been observed. The as-prepared films have good crystallinity related to the presence of Monoethanolamine in the solution and furnace annealing of the films at 400 °C has resulted in crystallinity improvement and a crystallite size increase of ~50%.

Drying with hot air flow ($T_h = 90–95$ °C) as the first step of the drying procedure and postdeposition irradiation with a nanosecond infrared laser (1064 nm, 100 mJ/cm^2) were used as tools for modification of the films structure and surface morphology. It has been found that the application of hot air drying gave some assistance to the effusion of organic remains and resulted in a better crystallinity of the two-step dried as-prepared films when compared with the crystallinity of the one-step dried films. Stripes (wrinkles) of various sizes have been revealed on the surface of as-prepared and annealed films produced by furnace drying at 140 °C. The stripes have been related to the existence of significant internal stress caused by fast solvent/MEA evaporation during drying. However, the surface of all samples prepared by using hot air drying was uniform which has been explained assuming that hot air drying retards the solvent evaporation, the film shrinkage is slowed up, which results in lower internal stress, uniform surface, and better lattice order. The Raman scattering results have revealed the subtle differences in ZnO nanostructure depending of film preparation procedure.

The XRD study shows that laser beam irradiation has given rise to slight variation in a crystallite size and mostly the increase of strain, whereas the analysis of Raman scattering data shows that laser-induced changes are most pronounced in as-grown samples produced by two-step drying procedure. Laser irradiation also leads to some decrease in the number of defects playing role of non-radiative carrier recombination centers, and reduces the size and density of small cracks and pores on the surface of as-prepared ZnO films produced by using hot air drying. These observations have been related to the transformation of a part of the quantum energy of the laser beam to heat and film annealing. The results of this investigation have shown that the application of hot air drying and irradiation with infrared pulse laser are promising for successful modification of the surface morphology and structure of sol–gel ZnO films.

Availability of data and material (data transparency)

All data described in the manuscript are available to all co-authors.

Code availability (software application or custom code)

Graphics program used: OriginPro 8.6.0 (64-bit) Sr3, Serial Number: GF3S5-6089-7606559, Registration ID: UHD-6YQ-8A1.
The AFM image analysis was done by means of Nanoscope 7.30 programme.

Acknowledgements RG-D gratefully acknowledge the financial support provided by the Bulgarian Ministry of Education and Science, National program "Young scientists and postdoctoral researchers" approved by DCM N577, 17.08.2018. DN and IB acknowledge the financial support provided by the European Regional Development Fund within the OP "Science and Education for Smart Growth 2014 - 2020", project No BG05M2OP001-1.001-0008. MS, MG-B, and ZP are thankful to the Institute of Physics, Belgrade and Ministry of Education, Science and Technological Development of the Republic of Serbia. All authors are thankful to the Bulgarian Academy of Sciences and Serbian Academy of Sciences and Arts (bilateral project "Preparation and characterization of nanostructured semiconductor thin films for sensor application").

Author contributions All authors whose names appear in the application have contributed significantly to the concept or design of the work; acquisition, analysis or interpretation of data.

Funding (information that explains whether and by whom the research was supported). RG-D gratefully acknowledge the financial support provided by the Bulgarian Ministry of Education and Science, National program "Young scientists and postdoctoral researchers" approved by DCM N577, 17.08.2018. DN and IB acknowledge the financial support provided by the European Regional Development Fund within the OP "Science and Education for Smart Growth 2014 - 2020", project No BG05M2OP001-1.001-0008. MS, MG-B and ZP are thankful to the Institute of Physics, Belgrade and Ministry of Education, Science and Technological Development of the Republic of Serbia. All authors are thankful to the Bulgarian Academy of Sciences and Serbian Academy of Sciences and Arts (bilateral project „Preparation and characterization of nanostructured semiconductor thin films for sensor application").

Compliance with ethical standards

Conflict of interest The authors declare no competing interests.

Publisher's note Springer Nature remains neutral with regard to jurisdictional claims in published maps and institutional affiliations.

References

1. Borysiewicz MA (2019) ZnO as a functional material, a review. Crystals 9:505–533. https://doi.org/10.3390/cryst9100505
2. Katayama M (1999) TFT-LCD technology. Thin Solid Films 341:140–147. https://doi.org/10.1016/S0040-6090(98)01519-3
3. Hung LS, Chen CH (2002) Recent progress of molecular organic electroluminescent materials and devices. Mater Sci Eng R 39:143–222. https://doi.org/10.1016/S0927-796X(02)00093-1
4. Rech B, Wagner H (1999) Potential of amorphous silicon for solar cells. Appl Phys A 69:155–167. https://doi.org/10.1007/s003390050986
5. Pauporte T, Lincot D (1999) Heteroepitaxial electrodeposition of zinc oxide films on gallium nitride. Appl Phys Lett 75:3817–3819. https://doi.org/10.1063/1.125466
6. Look DC (2001) Recent advances in ZnO materials and devices. Mater Sci Eng B 80(1-3):383–387. https://doi.org/10.1016/S0921-5107(00)00604-8
7. Özgür Ü, Alivov YI, Liu C, Teke A, Reshchikov MA, Doğan S, Avrutin V, Cho S-J, Morkoç H (2005) A comprehensive review of ZnO materials and devices. J Appl Phys 98:041301. https://doi.org/10.1063/1.1992666
8. Guziewicz E, Godlewski M, Krajewski T, Wachnicki Ł, Szczepanik A, Kopalko K, Wójcik-Głodowska A, Przeździecka E, Paszkowicz W, Łusakowska E, Kruszewski P, Huby N, Tallarida G, Ferrari S (2009) ZnO grown by atomic layer deposition: a material for transparent electronics and organic heterojunctions. J Appl Phys 105(12):122413. https://doi.org/10.1063/1.3133803
9. Muslih EY, Munir B (2018) In: Ameen S, Akhtar MS, Shin H-S (eds) Emerging solar energy materials. Intech Open Limited, London
10. Baruah S, Joydeep Dutta J (2009) Hydrothermal growth of ZnO nanostructures. Sci Technol Adv Mater 10:013001. https://doi.org/10.1088/1468-6996/10/1/013001
11. Wang J, Cui W, Zhu L, Wang J, Wei Q, Chen Z, Shan M, Yuan X, Hua J (2020) Structural, optical, and magnetic properties of low temperature hydrothermal synthesized (Gd, Al)-codoped ZnO nanoparticles. J Sol-Gel Sci Technol 93:193–201. https://doi.org/10.1007/s10971-019-05160-7
12. Znaidi L (2010) Sol-gel deposited ZnO thin films: a review. Mater Sci Eng B 174(1-3):18–30. https://doi.org/10.1016/j.mseb.2010.07.001
13. Kim HT, Lee S-Y, Park Ch (2017) Controls of surface morphology on sol-gel derived ZnO films under isothermal treatment conditions. Vacuum 143:312–315. https://doi.org/10.1016/j.vacuum.2017.06.034
14. Palneedi H, Park JH, Maurya D, Peddigari M, Hwang G-T, Annapureddy V, Kim J-W, Choi J-J, Hahn B-D, Priya S, Lee KJ, Ryu J (2018) Laser irradiation of metal oxide films and nanostructures: applications and advances. Adv Mater 30(14):1705148. https://doi.org/10.1002/adma.201705148
15. Lu H, Tu Y, Lin X, Fang B, Luo D, Laaksonen A (2010) Effects of laser irradiation on the structure and optical properties of ZnO thin films. Mater Lett 64:2072–2075. https://doi.org/10.1016/j.matlet.2010.06.022
16. Tsay C-Y, Wang M-C (2013) Structural and optical studies on sol–gel derived ZnO thin films by excimer laser annealing. Ceram Int 39:469–474. https://doi.org/10.1016/j.ceramint.2012.06.050
17. Hsiao W-T, Tseng S-F, Chung Ch-K, Chiang D, Huang K-Ch, Lin K-M, Li L–Y, Chen M-F (2015) Effect on structural, optical and electrical properties of aluminum-doped zinc oxide films using diode laser annealing. Opt Laser Technol 68:41–47. https://doi.org/10.1016/j.optlastec.2014.11.009
18. Zhao S, Hua Y, Chen R, Zhang J, Ji P (2016) Structural and electrical studies on ZnO-based thin films by laser irradiation. J Nanotechnol 2016:9385725. https://doi.org/10.1155/2016/9385725
19. Elhamali SO, Cranton WM, Kalfagiannis N, Hou X, Ranson R, Koutsogeorgis DC (2016) Enhanced electrical and optical properties of room temperature deposited Aluminium doped Zinc Oxide (AZO) thin films by excimer laser annealing. Opt Laser Eng 80:45–51. https://doi.org/10.1016/j.optlaseng.2015.12.010
20. Vajargah PH, Abdizadeh H, Ebrahimifard R, Golobostanfard MR (2013) Sol-gel derived ZnO thin films: effect of amino-additives. Appl Surf Sci 285B:732–743. https://doi.org/10.1016/j.apsusc.2013.08.118
21. Khan MI, Bhatti KA, Qindeel R, Alonizan N, Saeed Althobaiti H (2017) Characterizations of multilayer ZnO thin films deposited by sol-gel spin-coating technique. Results Phys 7:651–655. https://doi.org/10.1016/j.rinp.2016.12.029
22. Raoufi D, Raoufi T (2009) The effect of heat treatment on the physical properties of sol-gel derived ZnO thin films. Appl Surf Sci 255:5812–5817. https://doi.org/10.1016/j.apsusc.2009.01.010
23. Gegova-Dzhurkova R, Nesheva D, Mihailov V, Dzhurkov V, Terziyska P, Manolov E (2021) Effect of infrared laser irradiation on electrical conductivity and ethanol sensitivity of sol-gel ZnO thin films. J Phys Conf Ser 1762:012037. https://doi.org/10.1088/1742-6596/1762/1/012037

24. Musić S, Filipović-Vinceković N, Sekovanić L (2011) Precipitation of amorphous SiO_2 particles and their properties. Braz J Chem Eng 28:89–94. https://doi.org/10.1590/S0104-66322011000100011
25. Gao D, Zhang Z, Fu J, Xu Y, Qi J, Xue D (2009) Room-temperature ferromagnetism of pure ZnO nanoparticles. J Appl Phys 105:113928. https://doi.org/10.1063/1.3143103
26. Bindu P, Thomas S (2014) Estimation of lattice strain in ZnO nanoparticles: X-ray peak profile analysis. J Theor Appl Phys 8:123–134. https://doi.org/10.1007/s40094-014-0141-9
27. Moram MA, Vickers ME (2009) X-ray diffraction of III-nitrides. Rep Prog Phys 72:036502 (1–40). https://doi.org/10.1088/0034-4885/72/3/036502
28. Znaidi L, Touam T, Vrel D, Souded N, Yahia BS, Brinza O, Fischer A, Boudrioua A (2012) ZnO thin films synthesized by sol-gel process for photonic applications. Acta Phys Pol A 121:165–168. https://doi.org/10.12693/APhysPolA.121.165
29. Kaneva NV, Dushkin CD (2011) Preparation of nanocrystalline thin films of ZnO by sol-gel dip coating. Bulg Chem Commun 43:259–263
30. Sutanto H, Durri S, Wibowo S, Hadiyanto H, Hidayanto EE (2016) Rootlike morphology of ZnO:Al thin film deposited on amorphous glass substrate by Sol-gel method. Phys Res Int 2016:4749587. https://doi.org/10.1155/2016/4749587
31. Haas DE, Quijada JN, Picone SJ, Birnie III DP (2000) Effect of solvent evaporation rate on skin formation during spin-coating of complex solutions. Proc SPIE Sol-gel Opt V 3943:280–284. https://doi.org/10.1117/12.384348
32. Tsay Ch-Y, Fan K-SH, Wang Y-W, Chang Ch-j, Tseng Y-K, Lin Ch-K (2010) Transparent semiconductor zinc oxide thin films deposited on glass substrates by sol-gel process. Ceram Int 36:1791–179. https://doi.org/10.1016/j.ceramint.2010.03.005
33. Srikant V, Clarke DR (1998) On the optical band gap of zinc oxide. J Appl Phys 83:5447–5451. https://doi.org/10.1063/1.367375
34. Singh M, Singh M (2013) Thermal expansion in zinc oxide nanomaterials. Nanosci Nanotechnol Res 1:27–29. https://doi.org/10.12691/nnr-1-2-4
35. El-Kareh B (1995) Fundamentals of semiconductor processing technologies. Kluwer Academic Publishers, Boston
36. Šćepanović M, Grujić-Brojčin M, Vojisavljević K, Bernik S, Srećković T (2010) Raman study of structural disorder in ZnO nanopowders. J Raman Spectrosc 41:914–921. https://doi.org/10.1002/jrs.2546
37. Ashkenov N, Mbenkum BN, Bundesmann C, Riede V, Lorenz M, Spemann D, Kaidashev EM, Kasic A, Schubert M, Grundmann M, Wagner G, Neumann H, Darakchieva V, Arwin H, Monemar B (2003) Infrared dielectric functions and phonon modes of high-quality ZnO films. J Appl Phys 93:126–133. https://doi.org/10.1063/1.1526935
38. Alim K, Fonoberov VA, Shamsa M, Balandin AA (2005) Micro-Raman investigation of optical phonons in ZnO quantum dots. J Appl Phys 97:124313. https://doi.org/10.1063/1.1944222
39. Zielony E, Wierzbicka A, Szymon R, Pietrzyk MA, Placzek-Popko E (2021) Investigation of micro-strain in ZnO/(Cd, Zn)O multiple quantum well nanowires grown on Si by MBE. Appl Surf Sci 538:148061. https://doi.org/10.1016/j.apsusc.2020.148061
40. Harriman TA, Bi Z, Jia QX, Lucca DA (2013) Frequency shifts of the E_2^{high} Raman mode due to residual stress in epitaxial ZnO thin films. Appl Phys Lett 103:121904. https://doi.org/10.1063/1.4821222
41. Korepanov VI, Sedlovets DM (2018) Asymmetric fitting function for condensed-phase Raman spectroscopy. Analyst 143:2674–2679. https://doi.org/10.1039/C8AN00710A
42. Gruber TH, Prinz GM, Kirchner C, Kling R, Reuss F, Limmer W, Waag A (2004) Influences of biaxial strains on the vibrational and exciton energies in ZnO. J Appl Phys 96:289–293. https://doi.org/10.1063/1.1755433
43. Yu Y, Lin K, Zhou X, Wang H, Liu S, Ma X (2007) New C-H stretching vibrational spectral features in the Raman spectra of gaseous and liquid ethanol. J Phys Chem C 111:8971–8978. https://doi.org/10.1021/jp0675781
44. Horiba Jobin Yvon Raman Application note (2021) Raman Spectroscopy for Analysis and Monitoring. https://static.horiba.com/fileadmin/Horiba/Technology/Measurement_Techniques/Molecular_Spectroscopy/Raman_Spectroscopy/Raman_Academy/Raman_Tutorial/Raman_bands.pdf
45. Nateq MH, Ceccato R (2019) Enhanced sol–gel route to obtain a highly transparent and conductive aluminum-doped zinc oxide thin film. Materials 12:1744. https://doi.org/10.3390/ma12111744
46. Saravanan P, Gnanavelbabu A, Pandiyaraj P (2018) Effect of pre-annealing on thermal and optical properties of ZnO and Al–ZnO thin films. Int J Nanosci 17:1760017. https://doi.org/10.1142/S0219581X17600171
47. O'Reilly EP, Robertson J (1983) Theory of defects in vitreous silicon dioxide. Phys Rev B 27:3780–3795. https://doi.org/10.1103/PhysRevB.27.3780
48. Tohmon R, Shimogaichi Y, Munekuni S, Ohki Y, Hama Y (1989) Relation between the 1.9 eV luminescence and 4.8 eV absorption bands in high-purity silica glass. Appl Phys Lett 54:1650–1652. https://doi.org/10.1063/1.101396
49. Skuja L (1998) Optically active oxygen-deficiency-related centers in amorphous silicon dioxide. J Non-Cryst Solids 239:16–48. https://doi.org/10.1016/S0022-3093(98)00720-0
50. Skuja L, Hirano M, Hosono H, Kajihara K (2005) Defects in oxide glasses. Phys Status Solidi (c) 2:15–24. https://doi.org/10.1002/pssc.200460102
51. Gomi M, Oohira N, Ozaki K, Koyano M (2003) Photoluminescent and structural properties of precipitated ZnO fine particles. Jpn J Appl Phys 42(2R):481–485. https://doi.org/10.1143/JJAP.42.481
52. Djurišić AB, Leung YH, Tam KH, Hsu YF, Ding L, Ge WK, Zhong YC, Wong KS, Chan WK, Tam HL, Cheah KW, Kwok WM, Phillips DL (2007) Defect emissions in ZnO nanostructures. Nanotechnology 18:095702. https://doi.org/10.1088/0957-4484/18/9/095702
53. Musavi E, Khanlary M, Khakpour Z (2019) Red-orange photoluminescence emission of sol-gel dip-coated prepared ZnO and ZnO: Al nano-crystalline films. J Lumin 216:116696. https://doi.org/10.1016/j.jlumin.2019.116696